Journal of Applied Physics

RESEARCH ARTICLE | NOVEMBER 05 2025

A mobile high spatial-resolution muography instrument based on large-area Micromegas detectors

Special Collection: Muography: Discoveries, Innovations, and Applications

Yu Wang ; Shubin Liu ; Zhihang Yao ; Yulin Liu; Zhiyong Zhang ; Zhengyang He ; Ziwen Pan ; Changqing Feng

J. Appl. Phys. 138, 174902 (2025)
https://doi.org/10.1063/5.0288077

Journal of Applied Physics ARTICLE pubs.aip.org/aip/jap

A mobile high spatial-resolution muography instrument based on large-area Micromegas detectors

Cite as: J. Appl. Phys. **138**, 174902 (2025); doi: 10.1063/5.0288077
Submitted: 29 June 2025 · Accepted: 20 October 2025 ·
Published Online: 5 November 2025

Yu Wang,[1,2] Shubin Liu,[1,2,3,a)] Zhihang Yao,[1,3] Yulin Liu,[1,2] Zhiyong Zhang,[1,2] Zhengyang He,[1,2] Ziwen Pan,[1,2] and Changqing Feng[1,2]

AFFILIATIONS

[1]State Key Laboratory of Particle Detection and Electronics, University of Science and Technology of China, Hefei 230026, China
[2]Department of Modern Physics, University of Science and Technology of China, Hefei 230026, China
[3]School of Nuclear Science and Technology, University of Science and Technology of China, Hefei 230026, China

Note: This paper is part of the Special Topic on Muography: Discoveries, Innovations, and Applications.
[a)]**Author to whom correspondence should be addressed:** liushb@ustc.edu.cn

ABSTRACT

Muon radiography is an imaging technique based on muon absorption in matter that allows measurement of internal details in hidden objects or structures. This technique relies on measuring cosmic-ray muons tracks accurately, which reflects the incoming muon flux from both the target object and the open sky. In this paper, we report on the construction of a high spatial-resolution muography instrument based on Micromegas detectors. Using four layers of 400 × 400mm^2 Micromegas detectors, channel multiplexing circuits, and the versatile readout system, a movable muography instrument named μSTC-R400 was designed and constructed. Results show that the channel multiplexing circuits can resolve hit positions correctly, and the spatial resolution of the detector is approximately 190 μm. Experiments were conducted at an under-construction subway tunnel and outdoors near a mountain, demonstrating μSTC-R400's ability to maintain high spatial resolution outside the laboratory and its robustness in harsh environments.

I. INTRODUCTION

Cosmic-ray muon, with its strong penetrating power and naturally occurring, is an ideal probe for imaging the internal structure of large or well-shielded objects. Currently, muon imaging (muography) primarily employs two principles: muon transmission radiography and muon scattering tomography. This paper primarily focuses on muon transmission radiography, a technique based on the attenuation of muon flux as they pass through large structures, such as geological formations or man-made architectures. When a muon traverses a material, it experiences energy loss primarily through ionization and radiative processes. The mean energy loss rate can be described by the Bethe–Bloch and bremsstrahlung equations. For a thin layer dl of material with density $\rho(l)$, the energy loss primarily depends on the mass thickness, $\rho \times dl$. The fraction of muons crossing a material is, therefore, determined by the integrated density over the path length, as shown in Eq. (1), a quantity called opacity, also known as mass thickness,[1]

$$x(L) = \int_L \rho(l)dl = \bar{\rho} \times L. \quad (1)$$

The principle of the experimental measurement of the fraction of muons crossing a material is illustrated in Fig. 1, where the muon flux is measured by tracking detectors both toward the object [$N_{\text{object}}(\theta, \phi)$] and the open sky [$N_{\text{open-sky}}(\theta, \phi)$]. By calculating the ratio $N_{\text{object}}/N_{\text{open-sky}}$, the transmission ratio of cosmic-ray muons can be determined, which is expressed as

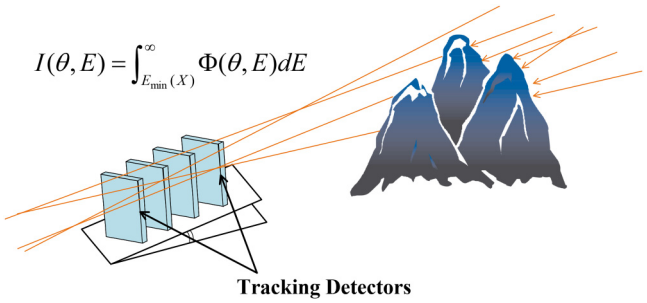

FIG. 1. Principle of muon radiography. A tracking system, typically an array of position-sensitive detectors, measures the incident muon flux. As muons traverse an object, their flux is attenuated due to absorption and scattering.

follows:

$$T(\theta,\phi)=\frac{N_{\text{object}}(\theta,\phi)}{N_{\text{open-sky}}(\theta,\phi)}=\frac{\int_{E_{\min}(X)}^{\infty}\Phi(\theta,E)dE}{\int_{E_0}^{\infty}\Phi(\theta,E)dE}. \quad (2)$$

Here, $\Phi(\theta, E)$ is the differential muon flux, $E_{\min}(x)$ is the minimum energy required for a muon to traverse an object with opacity x, and E_0 represents the minimum energy threshold for muons detected (e.g., determined by detector characteristics or analysis cuts). In experimental analysis, the differential muon flux $\Phi(\theta, E)$ is primarily dependent on the zenith angle θ. Therefore, the incident flux $\Phi(\theta, E)$ is considered to be the same for both the open-sky and object measurements within the same angular bin.

This transmission ratio is directly linked to the energy loss experienced by muons, which, in turn, depends on the material's opacity. Consequently, for a muon to traverse a material of a given opacity $x(L)$, it must possess minimum initial energy, E_{min}. Once E_{min} is determined, the opacity x can be calculated. Subsequently, the average density $\bar{\rho}$ can be obtained if the physical length L of the object is known.

To convert the measured transmission ratio T into opacity x (and subsequently density), several approaches are commonly employed to model the muon spectrum. These include comprehensive Monte Carlo simulations of cosmic-ray air showers [such as those performed with CORSIKA (COsmic Ray Simulations for KAscade)[2]], which can generate detailed muon energy and angular distributions. Empirical models, derived from experimental data, are also used; for instance, the EcoMug library[3] is based on measurements from Altazimuthal Detector for AtMospheric Cosmic-Ray Observation (ADAMO) detectors.[4] Additionally, some methods utilize analytical calculations of pion and kaon decay to generate the energy spectrum of cosmic-ray muons, with notable examples, including models proposed by Gaisser[5] and Bugaev *et al.*[6] Hebbeker *et al.* further refined these by combining Bugaev's spectrum with experimental data.[7] Alternatively, for simpler analyses or specific experimental conditions, the energy loss rate can be approximated as a constant. For instance, in the DIAPHANE experiment,[8] the muon energy loss in rock was set at 2.5 MeV cm^2/g.

The first application of muon radiography was the measurement of the overburden mass of the Guthega–Munyang tunnel using a Geiger counterarray as the sensitive detectors.[9] Subsequently, in the 1960s, L. W. Alvarez explored the possibility of searching for hidden chambers within the Second Pyramid of Giza.[10] Over the past three decades, numerous experiments have been conducted in areas, such as volcano imaging,[11–14] geological surveying,[15–17] and detection of cavities for archaeological[18] and civil engineering applications.[19,20] A notable recent example is the discovery of a big void in Khufu's Pyramid with the combination of nuclear emulsion chambers, plastic scintillator detectors, and Micromegas detectors.[21]

The key aspect of muography is the accurate measurement of muon tracks. Except the nuclear emulsion chambers, most detection methods employ multiple layers of detectors to reconstruct these tracks. The use of finer resolution detectors can obtain more accurate results and contribute to a more compact design. Spatial resolution and detection area are two critical parameters for optimizing imaging time and accuracy. Imaging time is determined by the number of muons that penetrate the object and are subsequently recorded by the detectors. A muography instrument with a larger detector area has a greater acceptance, allowing the detection of muons from a wider range of directions, which helps to maintain a reasonable experimental duration.

The most common detector type employed in muography is the scintillator with Silicon Photomultiplier (SiPM) readout.[8,22–25] A typical scintillator telescope consists of two or more double layers of orthogonal plastic scintillator bars, used to measure muons tracks in two independent projection directions. For rectangular bars, where a single muon typically produces a hit in one scintillator bar, the spatial resolution σ is related to the bar's lateral width L by $\sigma = L/\sqrt{12}$, assuming a uniform distribution of hit positions within the bar.[26] For triangular-shaped bars, spatial resolution can be improved by measuring the signal fraction in adjacent bars, achieving approximately 3 mm resolution for a bar with 1.7 cm height and 3.3 cm width.[25]

With advancements in nuclear instrumentation, micro-pattern gaseous detectors (MPGDs) have become a feasible option for muon radiography applications, as demonstrated by their uses in imaging Khufu's Pyramid[21] and the WatTo experiment.[27] These detectors can achieve a spatial resolution of a few hundred micrometers at a reasonable cost. In particular, the Micromegas (Micro-MEsh Gaseous Structure) detector can achieve a spatial resolution of approximately 100 μm over active areas of up to several thousands square centimeters. However, a large detection area combined with fine spatial resolution increases the complexity of the readout system design. This challenge can be mitigated through specially designed channel multiplexing methods, which reduce the number of required readout channels while preserving spatial information, achieving a balance between the detection area and readout complexity.[28–32] On the other hand, gaseous detectors are often considered less suitable for field applications outside the laboratory due to their requirement for a continuous gas supply and their susceptibility to discharge caused by environmental factors, such as vapor or dust pollution. These issues can be addressed by carefully controlling the gas flow and by robustly enclosing the detectors.

In this paper, a high spatial-resolution muon radiography instrument based on thermal-bonding Micromegas detectors is developed and presented. The sensitive area of this detector is 400×400 mm^2, and the number of anode strips is 2000 for a single detector with two dimension readout. To achieve a compact instrument design, a novel channel multiplexing method and highly integrated front-end electronics cards have been implemented in this system. This detector achieves a spatial resolution better than 200 μm with the implemented multiplexing circuit and front-end electronics. Subsequently, we performed muon radiography experiments in a subway tunnel under construction, and an outdoor environment near a mountain, demonstrating the capability and stability of this instrument.

II. SYSTEM DESIGN AND AN EXPERIMENTAL SETUP

The muography instrument consists of four layers of Micromegas detectors serving as sensitive elements, channel multiplexing circuits to reduce readout electronics requirements, Front-end Electronics Cards (FECs) for signal amplification and digitization, and back-end electronics for event identification and data concentration.

A. Resistive Micromegas detector

The Micromegas detector is a typical micro-pattern gaseous detector operating in a proportional mode, featuring a drift region and a thin amplification gap structure. A simplified cross-sectional structure of the Micromegas is shown in Fig. 2. The active volume is separated into a drift region, where the incident particle ionizes the working gas, and an amplification gap, where the primary ionizations are multiplied through the avalanche process.

The distance between the drift cathode and the mesh electrode of our detector is 5 mm, and the thickness of the amplification gap is approximately 100 μm. A germanium layer coated on the surface of the anode PCB (Printed Circuit Board) serves as a resistive anode and is connected to the GND. The conversion-drift electric field is established by applying negative voltages to the mesh electrode and a slightly higher voltage to the drift cathode.

When a muon enters the detector, primary ionization is generated. The strong electric field in the amplification region draws the primary electrons through the mesh voids and initiates the avalanche process. The signal induced on the anode strips is a sum of the electrons and ions signal, and this signal, when read out by a low-noise charge-sensitive preamplifier, is primarily due to the positive ion drift toward the micromesh electrode.

As shown in Fig. 3, the readout strips were designed in the second and third layers of the PCB with an orthogonal arrangement. This design makes a single active volume to measure both X and Y hit positions. The strip pitch is 400 μm, with the width of strips in the upper layer being 68 μm and those in the lower layer being 295 μm.

In contrast to conventional Micromegas fabrication methods, such as the bulk method based on photoetching processes, we employed a thermal-bonding method. In this approach, small spacers made of a thermal-bonding film are placed on the anode PCB to support the tensile mesh electrode. Further details about the Micromegas detector can be found in this work,[33] where the detector design was enlarged for the present work.

Several detectors with different dimensions were designed and implemented. In this paper, detectors with sensitive areas of 400×400 mm^2 are used to construct the muon radiography instrument. A photograph of the Micromegas detector is shown in Fig. 4.

B. Channel multiplexing circuit

A major constraint in the application of high spatial-resolution Micromegas detectors is the requirement for a large number of readout channels, leading to increased cost, power consumption, and data processing complexity. For example, the Micromegas detector used in this work has 2000 anode strips (1000 for X and 1000 for Y dimensions), which would typically require 2000 readout channels. For a muon radiography instrument with four layers of detectors, the total number of strips requiring readout could reach 8000. To address this challenge, we proposed a position-encoded multiplexing method, in which each front-end electronics channel reads out multiple detector strips.

The fundamental principle of this multiplexing approach is that within a single acquisition window (typically set to a few microseconds or less), at most one muon will hit the detector, which is critical to avoid ambiguities in hit reconstruction. The

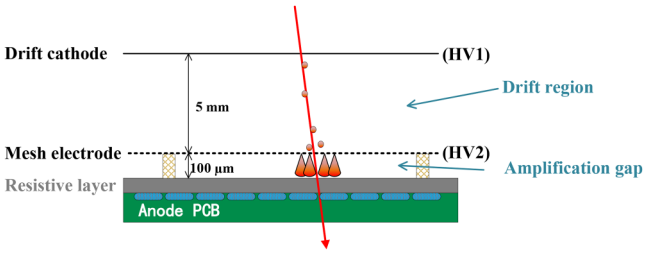

FIG. 2. Simplified cross-sectional structure of the Micromegas detector. Note that the thicknesses of the drift region and the amplification gap are not drawn to scale.

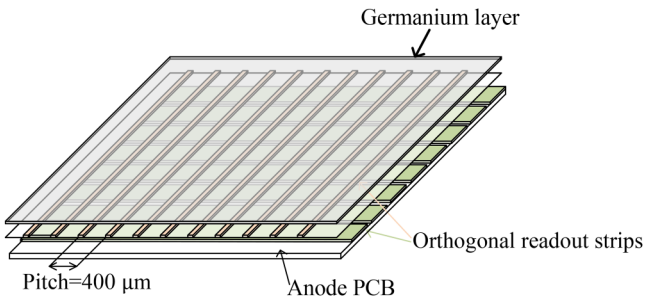

FIG. 3. Structure of the readout strips on the anode PCB, where the second and third layers form the orthogonal readout strips. The germanium layer is coated after PCB manufacture.

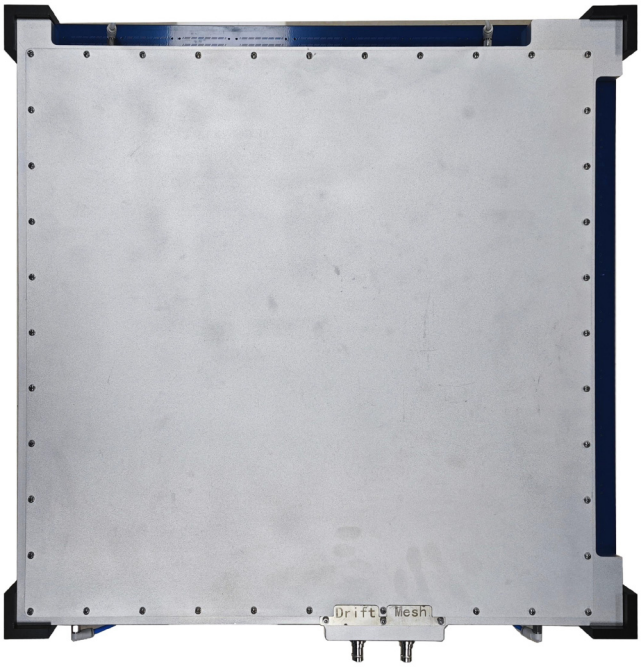

FIG. 4. Photograph of the Micromegas detector (400 × 400 mm^2) used in this research.

resulting ionization charges distribute over several adjacent strips for each dimension, near the hit point. Therefore, a specially designed mapping relation can be implemented, where each contiguous group of strips of the detector in the same layer is connected to a unique pair of readout electronics channels. When signals are read back on a specific group of multiplexed readout channels, multiple potential hit locations on the detector could be inferred. However, according to the mapping relationship, only one result corresponds to contiguous strips, which is the actual hit location on the detector. A mathematical model for this approach was established in our previous work, where different types of multiplexing circuits were designed and evaluated.[32]

In this work, we employ a circuit with a multiplexing factor of eight, where 512 detector strips are multiplexed into 64 front-end electronics channels. The encoding circuit is shown in Fig. 5. For each dimension of the detector strips, two multiplexing circuits are used, meaning that 1024 strips of the detector are read out by 128 channels of electronics.

C. Front-end electronics card (FEC)

The readout is handled by an FEC, which adopts a design that was verified in the PandaX III (Particle AND Astrophysical Xenon experiment III) project.[34] The key differences lie in the use of an upgraded version of the readout ASIC named STAGE (SEcond stAGe of the AGET[35,36]) and the utilization of channel hit information for self-trigger signal generation.

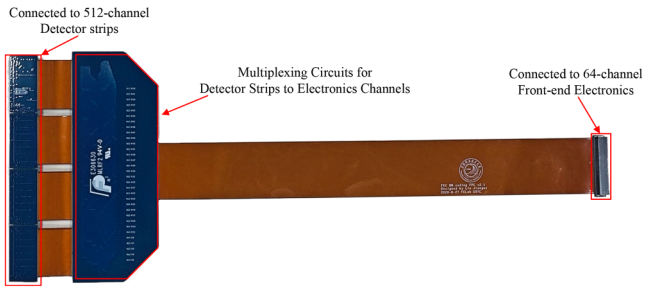

FIG. 5. Photograph of the multiplexing circuit that connects 512 detector strips to 64 readout electronics channels.

The structure of the STAGE chip is shown in Fig. 6. It has 64 active channels, which process the signals from the Micromegas detector after channel multiplexing, and 4 dummy channels, which are not connected to the detector but serve as noise monitors for the chip. Each channel consists of a charge-sensitive amplifier (CSA), a pole-zero canceler (PZC), an analog shaper (S&K Filter, Sallen–Key Filter), a discriminator for trigger generation, and a 512-cell switched capacitor array (SCA). The amplified and shaped signal is sampled by the SCA and then sent out of the chip under the control of the field-programmable gate array (FPGA) on the FEC. The trigger signal from each channel contributes to the total trigger signal, with the amplitude proportional to the number of channels exceeding the on-chip threshold.

A single FEC uses four STAGE chips to sample the encoded signals, with one FEC reading out exactly one layer of the detector. The output of each STAGE chip is digitized by a single-channel 12-bit analog-to-digital converter (ADC) and processed by the FPGA. A channel-specific threshold is set to suppress the idle channels. All digitized data with values greater than the preset thresholds, along with timestamp, trigger number, and checksum, are constructed into a user-defined data frame and transmitted to the back-end data acquisition (DAQ) board.

D. Back-end electronics and remote control

A back-end electronics card designed for small to medium-scale physics experiments is adopted in the construction of this muography instrument.[37] It performs data gathering from the FECs, event identification of potential muons, and data transmission to the host PC.

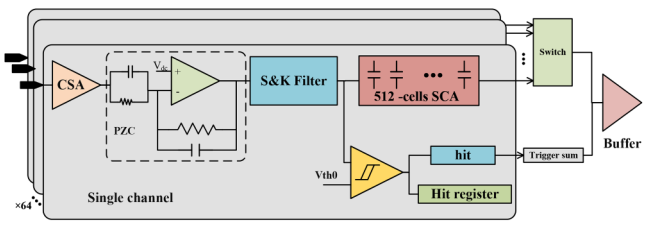

FIG. 6. Block diagram of the STAGE chip.

The back-end electronics card communicates with the FECs via optical fiber interfaces using a custom-defined protocol. With the time domain multiplexing (TDM) method, the link between the back-end electronics and FECs is divided into three virtual channels for trigger, data, and command transmission.

For remote control, a 4G modem provides Internet access to the instrument. A Windows Subsystem for Linux (WSL) based automatic data processing procedure performs data processing and transmission to the laboratory server. Manual control, remote debugging, and testing are performed via Windows Remote Desktop through a ZeroTier network.

E. Self-trigger mode

A self-trigger mode was developed to select potential muon signals, while the instrument operates in a continuous mode. This mode consists two main parts: pre-trigger generation by the FECs, which indicates the detection of overthreshold signals, and subsequent valid trigger generation by the back-end electronics after performing trigger selection.

The pre-trigger signal is generated through two stages in the FEC. The first stage is implemented using the built-in "multiplicity" function of the ASIC.[36] As shown in Fig. 6, during the acquisition phase, the shaped signal is continuously sampled by the SCA and simultaneously compared with a programmable voltage threshold. If the signal exceeds the threshold, a single-channel hit signal is generated. A total trigger signal is then produced based on the single-channel hit signals in an analog mode, with an amplitude proportional to the number of single-channel hits. This total trigger signal (referred to as the multiplicity signal, which indicates how many channels are overthreshold) is amplified to the differential analog output ports and continuously acquired by the on-board ADC. A second-stage trigger is generated by applying two thresholds to identify valid multiplicity signals: a lower one to suppress triggers caused by noise and a higher one to eliminate spurious triggers resulting from discharges in the Micromegas detectors. When the multiplicity signal falls between the lower threshold and the higher threshold, a potential event is detected, and the FEC sends a pre-trigger signal to the back-end electronics.

The back-end electronics records pre-trigger signals from each FEC and maintains them for a programmable time period, after which the register is cleared. If the recorded pre-triggers match the configured trigger pattern, a fast trigger signal followed by a 32-bit trigger ID is distributed to all FECs. The trigger pattern is configurable via control commands. In this specific application, a valid trigger is generated and sent to the FECs if at least three layers of FECs generate a pre-trigger signal. Upon receiving the fast trigger signal, the FECs stop the acquisition phase and controls the ASICs to sequentially output the sampled analog signals from the SCAs for conversion. The digitized data are compared against the preset channel-specific thresholds, and only data exceeding these thresholds are packaged and transmitted to the back-end electronics.

F. Construction of the instrument

A muon radiography instrument was constructed using these detectors and electronics cards and named μSTC-R400 (muon Scattering and Transmission imaging faCility, utilizing $400 \times 400\,\mathrm{mm}^2$ detectors for radiography). As shown in Fig. 7, this radiography instrument contains 4 layers of Micromegas detectors, 16 multiplexing circuits (4 for each layer), 4 FECs, a back-end electronics card, a mini-PC, 2 high-voltage (HV) modules housed in a mini-NIM case, and a remote-controlled Ackerman chassis to support the entire system. The system's orientation, including its zenith and azimuthal angles, is controlled by two motors, allowing for a precise adjustment of the viewing direction toward target objects.

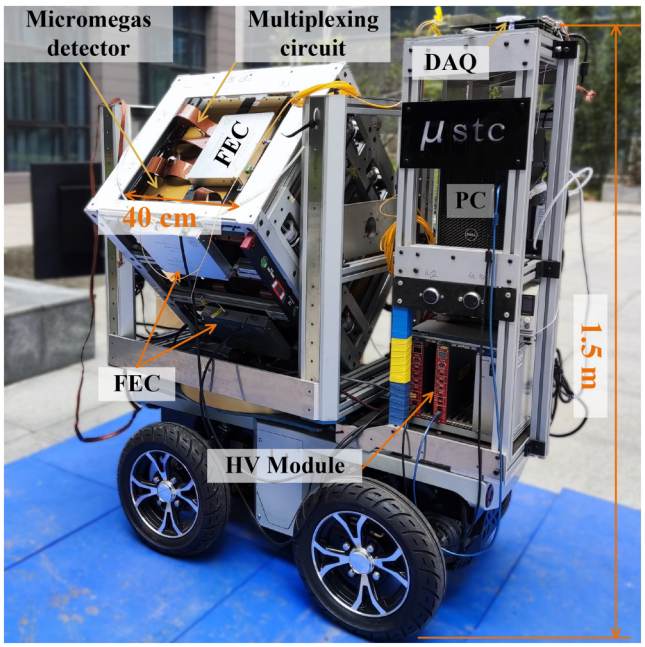

FIG. 7. Photograph of μSTC-R400. The constructed system includes Micromegas detectors, a multiplexing circuit, FECs, back-end electronics (DAQ) card, PC, HV modules, and the four-wheel chassis.

III. EXPERIMENTAL RESULTS

A. Performance of the readout electronics

The readout electronics cards were calibrated before installation into μSTC-R400. In the calibration, a charge signal was generated by applying a step-down voltage through a 1 pF capacitor in series and fed into the calibration pin of the ASICs (In_cal input). With the dynamic range set to 120 fC and a peaking time of 1039 ns, the charge-to-ADC conversion gain is approximately 29 ADC units/fC. Under this calibration relationship, the root mean square (RMS) value of the equivalent noise charge (ENC) for all channels connected to the detector via channel multiplexing circuits is shown in Fig. 8, with 95% of the FEC channels exhibiting noise less than 0.78 fC.

B. Energy spectrum and position decoding

The detectors operate in a gas-flow mode, with the working gas being a mixture of argon and 7% carbon dioxide. In our

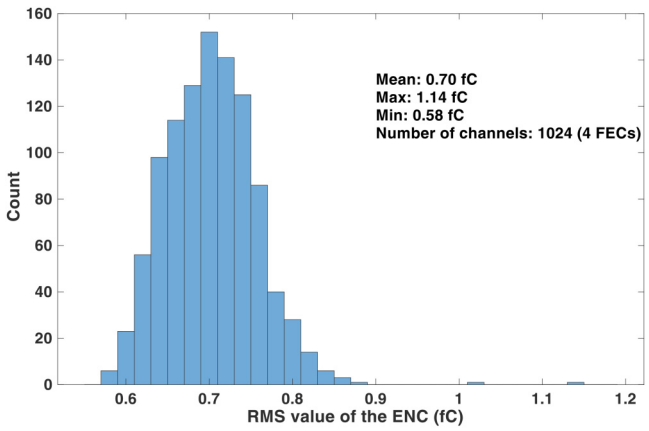

FIG. 8. Distribution of the RMS noise of the FECs connected to the detector.

experiments, the gas flow was set to 25 ml/min, and the working voltages of the drift cathode and mesh were set to −570 and −720 V, respectively.

Each cosmic-ray muon deposits energy in the drift area, generating ionization. This ionization is avalanched in the amplification gap, generating induction signals on the readout strips in both X- and Y-directions. By summing the charges on the adjacent strips for each valid event, the cosmic ray energy deposition spectrum is obtained and shown in Fig. 9. The charge distribution mainly follows the expected Landau distribution. After performing a Landau–Gaussian convolution fit using ROOT, the peak value is approximately 125 fC.

Since the strips of the detectors are multiplexed, the hit positions can be decoded when more than one readout electronics

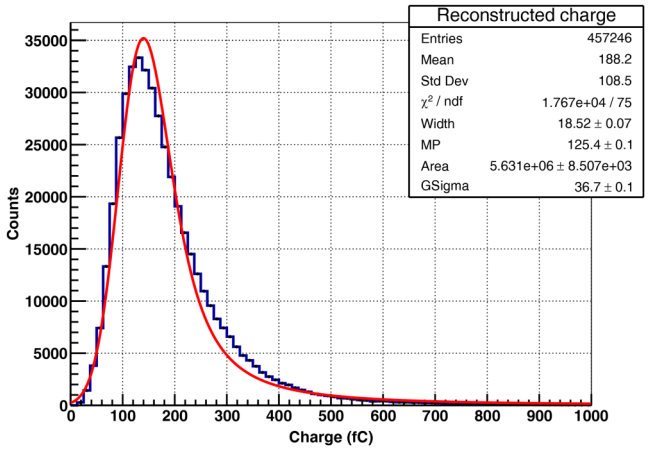

FIG. 9. Energy deposition spectrum of cosmic-ray muons measured by the detector, where the blue line with block asterisks represents the measured and reconstructed data, and the red line represents the convoluted Landau and Gaussian fit.

channel reads out valid signals. Figure 10 shows the distribution of the number of channels exceeding thresholds in each event. This result indicates that the position encoding multiplexing method can achieve nearly lossless channel compression in this muography instrument.

C. Spatial resolution and angular resolution

The principle of calculating the spatial resolution of the instrument is shown in Fig. 11. One of the layers is designated as the target layer, and the hit positions from the other three layers are used to fit a reference track. The fitting result can be expressed as $x_{fit} = k_x \times z_t + b_x$, where k_x and b_x are the slope and intercept of the fitting track, respectively, and z_t is the z coordinate of the target layer. After detector alignment to correct the installation offsets and rotations, the deviation $\Delta x = x_{hit} - x_{fit}$ can be calculated, where x_{hit} is the hit position measured by the target detector. By statistically analyzing a large number of muon tracks, the distribution of Δx can be obtained and fitted with a double Gaussian function. Figure 12 shows the fitting result of the Δx in the X direction of the inner layer detector with an incident angle range of 0°–5°. The narrow component of the Gaussian distribution (blue line) has a standard deviation of 0.188 mm. The spatial resolution of the instrument is defined as the standard deviation of the Δx distribution. This resolution can be conceptually divided into two contributing factors: the uncertainty from trajectory fitting [$\sigma(x_{\text{fit}})$] and the intrinsic residual of the detector under test [$\sigma(x_{\text{hit}})$]. In muography applications, both these components contribute to the overall precision of muon track measurement, and their combined effect represents the spatial resolution of the instrument.

Regarding angular resolution, the muon track is reconstructed by fitting the hit points from four layers. The track can then be represented by a direction vector $\vec{D}(k_x, k_y, 1)$ and a point $P(x_0, y_0, 0)$, where k_x and k_y are calculated as

$$k_x = \frac{\sum_{j=1}^{n}(z_j - \bar{z})x_j}{\sum_1^n (z_j - \bar{z})^2}, \quad k_y = \frac{\sum_{j=1}^{n}(z_j - \bar{z})y_j}{\sum_1^n (z_j - \bar{z})^2}, \tag{3}$$

where n is the number of fitted detectors and (x_i, y_i, z_i) are the hit points for each detector. Note that the z_i coordinates are fixed after the instrument's construction; for our four layers, these are 0, 167, 395, and 587 mm.

Thus, the reconstructed angles are given by $\theta = \arctan\sqrt{k_x^2 + k_y^2}$ and $\phi = \arctan(k_y/k_x)$, where θ and ϕ are the zenith and azimuthal angles, respectively. The angular resolution of θ can, thus, be written as

$$\Delta\theta = \frac{1}{1 + k_x^2 + k_y^2} \times \sqrt{\left(\Delta k_x^2 + \Delta k_y^2\right)}, \tag{4}$$

where Δk_x and Δk_y can be calculated from Eq. (3). Assuming all detectors have similar performance, Δk_x can be approximated as $\Delta k_x = \Delta x / \sqrt{\sum_1^n (z_j - \bar{z})^2}$. Given that k_x and k_y can be minimal (approaching zero for near-vertical tracks) and assuming similar

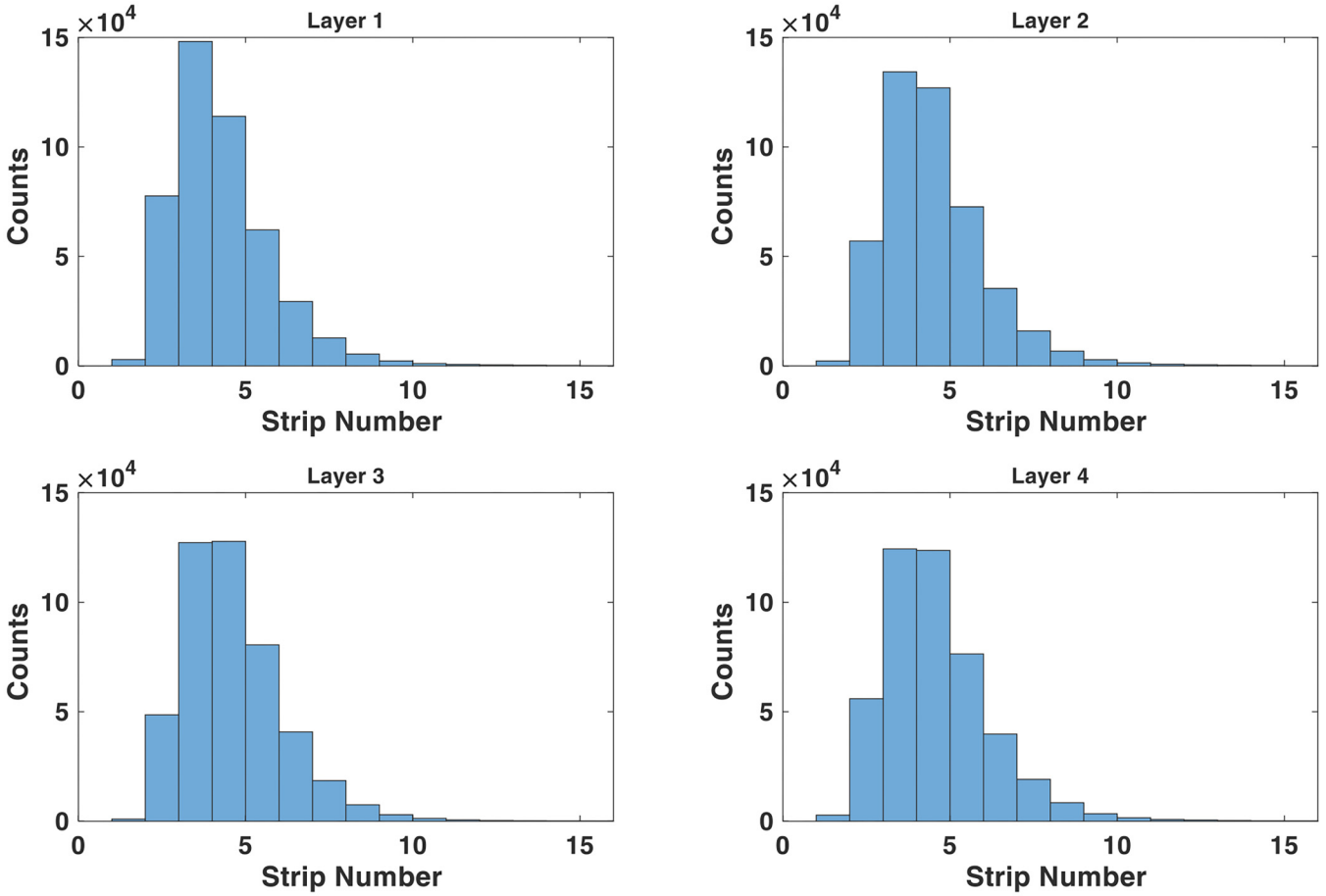

FIG. 10. Distribution of the number of channels exceeding thresholds in each event.

resolution along the X and Y dimensions, the overall angular resolution $\Delta\theta$ can be estimated as $\sqrt{2}\Delta k_x$. For the μSTC-R400, the angular resolution is approximately 0.6 mrad.

D. Muon radiography experiment results

1. Measurement at an underground tunnel

An experiment was performed at a subway tunnel under construction in the Hefei city. As shown in Fig. 13, μSTC-R400 was placed in the subway tunnel approximately 18 m below the ground surface. A river on the ground flows above the subway tunnel, approximately perpendicular to it. According to the engineering investigation, the vertical distance between the riverbed and the bottom of the tunnel is about 11 m. Since the subway site was under construction during the experiment, a UPS module was used to prevent power surges and sudden power loss. Remote control was implemented via the local WiFi network in the tunnel for monitoring the status of detectors and readout electronics.

The measurement in the tunnel lasted approximately 300 h, while an open-sky muon flux measurement conducted at a ground level on the USTC campus lasted about 266 h. After performing position alignment to correct for offset and rotation

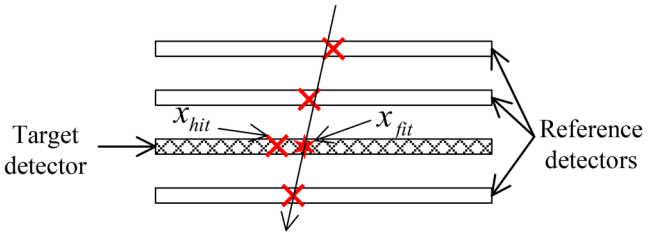

FIG. 11. Illustration of the method for calculating spatial resolution. The actual hit positions are represented by red crosses, while the fit hit position is indicated by a red hexagram.

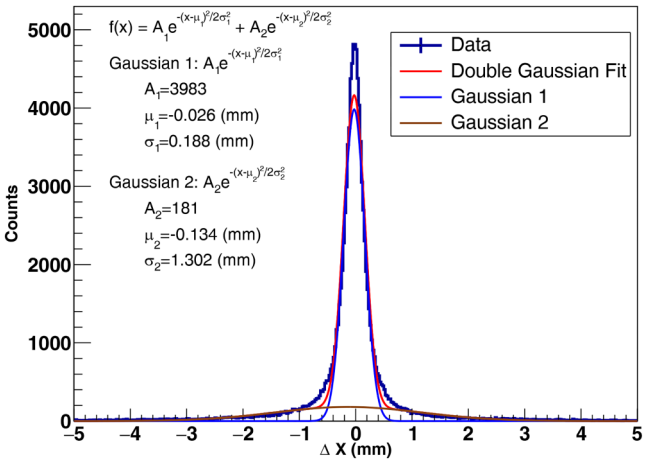

FIG. 12. Deviation distributions of the Micromegas in the X direction with an incident angle range of 0°–5°.

errors, muon tracks were reconstructed where all four layers of detectors were fired and the RMSE (Root Mean Square Error) of the fitted tracks was less than 2 mm. Figures 14(a) and 14(b) show the 2D hit distributions measured on the ground (the open sky) and in the tunnel, respectively, with the muon counts normalized to 10 min. Figure 14(c) presents the transmission map for the subway tunnel measurement. Figure 15 shows the distributions of the θ and ϕ angles for open-sky and tunnel measurements (counts normalized to 10 min). Results show that the muon flux is attenuated by the soil above the tunnel, while the influence of the river is not significant. This can be attributed to the limited density difference between the river water and the surrounding overburden soil. Nonetheless, μSTC-R400 has demonstrated its robustness by operating successfully in the subway tunnel environment where vapor and dust were present during the test.

2. Measurement at a mountain

To validate the versatility of this muography instrument in outdoor environments, an experiment was performed at

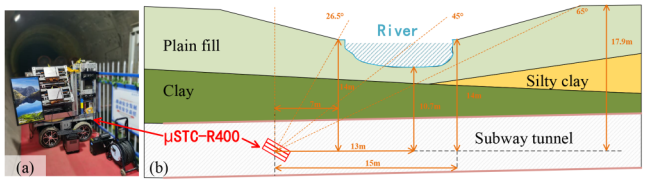

FIG. 13. (a) Photograph of the μSTC-R400 instrument in the under-construction subway tunnel with a zenith angle of 30° and oriented toward the river on the ground surface. The direction of the river is approximately perpendicular to the subway tunnel. (b) Placement of the detector in the underground tunnel and the cross section of the stratum from an engineering investigation.

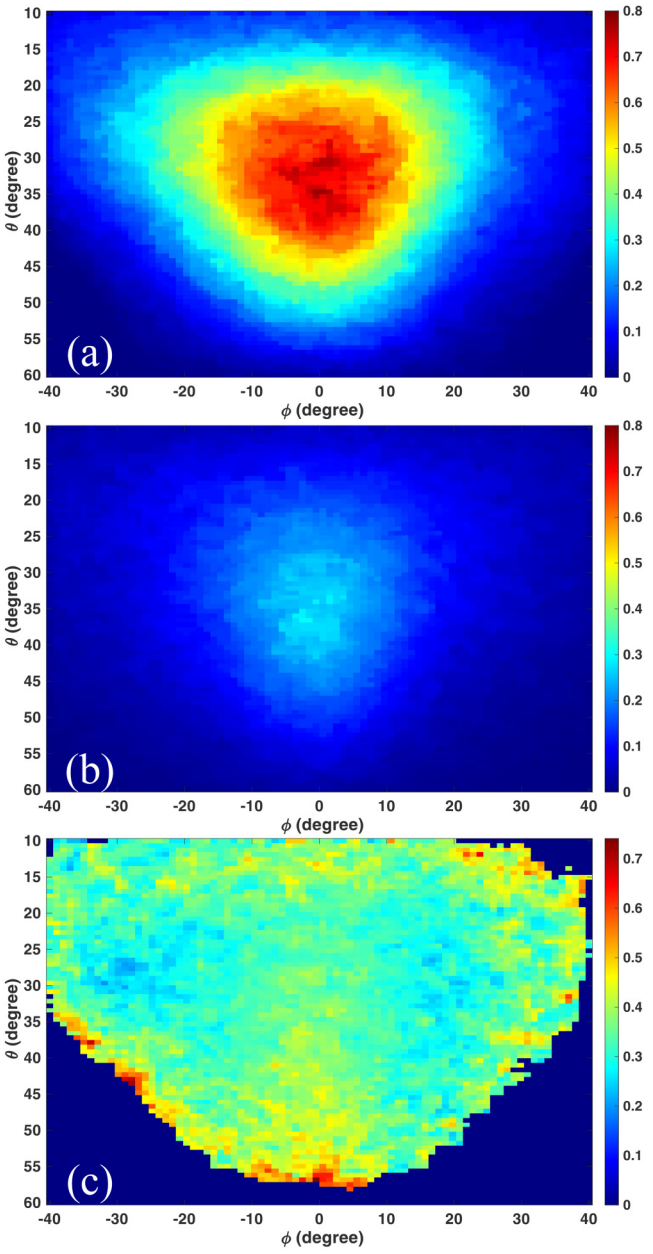

FIG. 14. (a) 2D hit distribution for open-sky measurements. (b) 2D hit distribution measured in the tunnel. The color bars in (a) and (b) represent the muon count per 10 min. (c) Transmission map calculated as the ratio of (b) to (a). To suppress statistical noise in low-count regions, pixels with muon counts below 5% of the maximum are masked (set to zero).

Dashu Mountain in the Shushan Forest Park located in the urban area of Hefei city. As shown in Figs. 16(a) and 16(b), μSTC-R400 was placed in a microbus positioned near the foot of the mountain. The horizontal distance between the

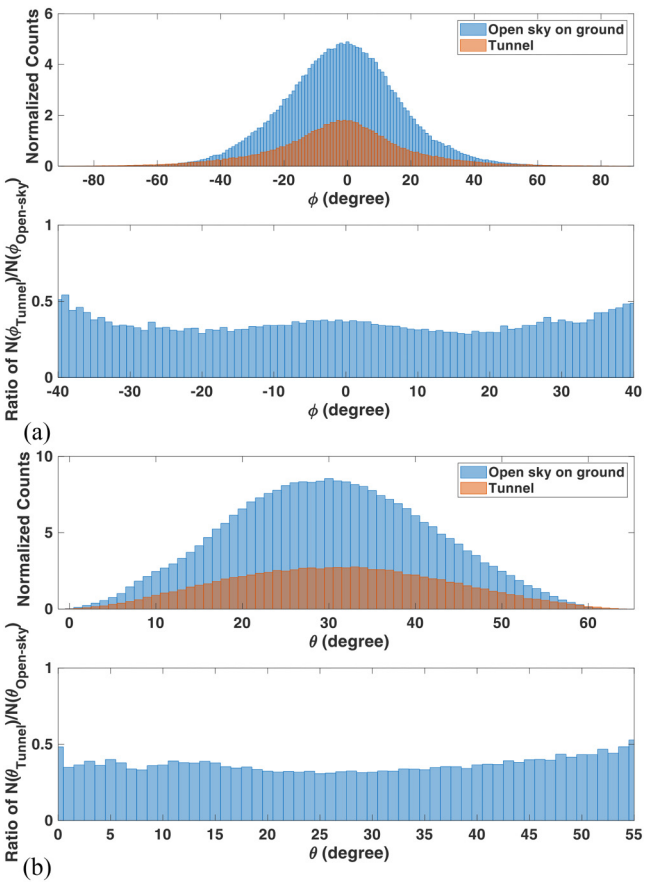

FIG. 15. (a) Distribution of the θ angle and the ratio $\theta(N_{\text{tunnel}})/\theta(N_{\text{open-sky}})$. (b) Distribution of the ϕ angle and the ratio $\phi(N_{\text{tunnel}})/\phi(N_{\text{open-sky}})$.

instrument and the top of the Dashu Mountain is approximately 1 km, with a vertical distance of about 200 m. To measure both the open-sky muon flux and the flux through the mountain at the same time, the detectors were rotated so that their normal was parallel to the ground, with the center approximately pointing toward the mountain peak. As shown in Fig. 16(c), the detectors could simultaneously record muons from both the mountain direction and the open sky. This configuration ensured that fluctuations in muon flux and detector gain remained equal for both the target measurement and the background measurement.

The test continued for approximately 37 days, during which a heavy snowfall occurred in Hefei; yet, the instrument maintained proper functioning. The 2D distribution of muons from the open-sky direction and from the mountain direction is shown in Figs. 17(a) and 17(b), where the "shadow" caused by the mountain's absorption is clearly visible. Figure 17(c) shows the transmission ratio, where values larger than 1.2 were set to 1.2 to provide clear color gradation. The shape of the Dashu Mountain was obtained through drone mapping with an accuracy of 10 m, and Fig. 17(d) shows the traversal length at the experiment site.

With the known transmission rate $T(\theta, \phi)$, the traversal length $L(\theta, \phi)$, and according to Eq. (1), the average density of the object can be calculated as $\bar{\rho}(\theta, \phi) = X(\theta, \phi|E_{\text{min}})/L(\theta, \phi)$, where E_{min} is the minimum energy required to traverse the objects. The reconstructed density is shown in Fig. 17(e) using parameters from the EcoMug library[3] and from this work,[8] with the mountain body treated as rock with $E_{\text{min}} = 2.5\,\text{MeV}\,\text{g}^{-1}\,\text{cm}^2 \times X$. The reconstructed density values are lower than expected empirical values. This discrepancy may be attributed to uncertainties in the determination of E_{min} at large incident angles, as well as the 10 m accuracy of the traversal length measurement obtained from drone mapping.

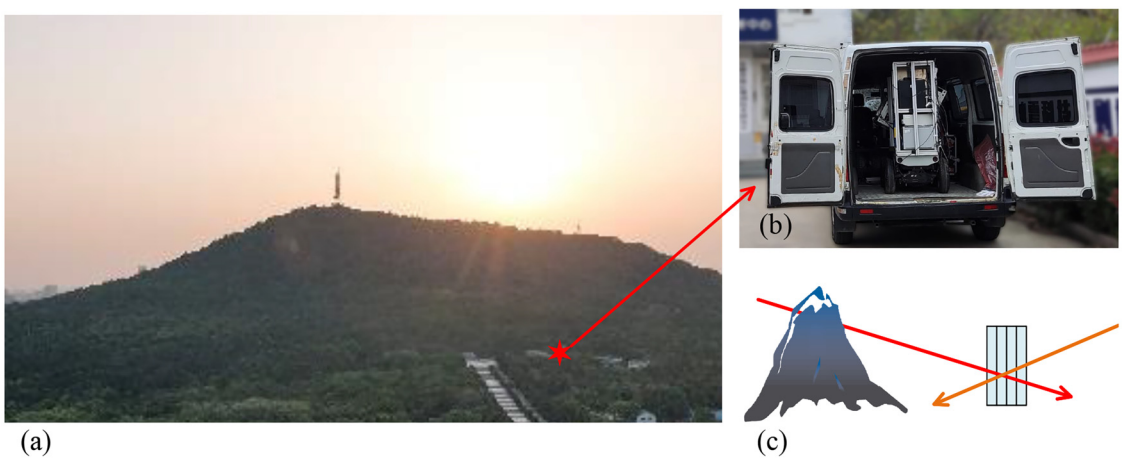

FIG. 16. (a) View of the Dashu Mountain, with μSTC-R400 placed at the foot of the mountain [approximately at the location marked by the hexagram (with the GPS location at 117.18°E 31.84°N 74.7 m)). (b) Photograph of the instrument placed in a microbus. (c) Diagram of the detector placement, where the normal of the detector is parallel to the ground.

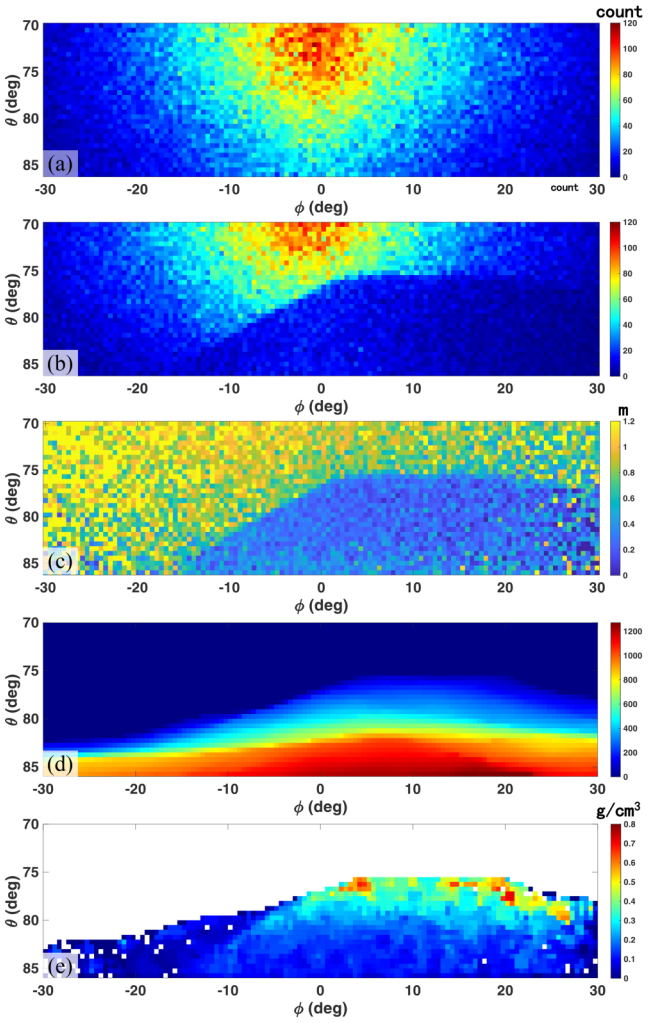

FIG. 17. (a) 2D hit distribution from the open-sky direction. (b) 2D hit distribution from the mountain direction. (c) Transmission ratio calculated as $N_{\text{mountain}}/N_{\text{open-sky}}$ with values larger than 1.2 set to 1.2. (d) Traversal length from the experiment site perspective. (e) Reconstructed density using a constant minimum transmission energy of 2.5 MeV g^{-1} cm^2 × X.

IV. DISCUSSION AND CONCLUSIONS

In this study, a high spatial-resolution muon radiography instrument named μSTC-R400 was designed and implemented. Four layers of detectors with a sensitive area of 400 × 400 mm^2 were used, requiring a total of 8000 strips to be read out. A channel multiplexing method was applied to reduce the large number of readout channels. Together with the scalable readout system and the self-trigger mode, this instrument could be constructed in a relatively compact size. Test results show that the RMS of the ENC is approximately 0.8 fC with a dynamic range of 0 ∼ 120 fC, which adequately covers the signal range of the Micromegas detector. The spatial resolution of the detectors with encoding readout is approximately 190 μm, which provides sufficient angular resolution for muon radiography. The long-term stability and the environmental suitability were tested during different types of experiments in harsh environments, demonstrating that with proper design and sealing, the Micromegas detectors can operate effectively in muography experiments outside the laboratory. The instrument presented in this article indicates that Micromegas detectors with the thermal-bonding method can be a promising solution for building high spatial-resolution muography facilities, while the channel multiplexing readout circuit significantly reduces system complexity.

Current research and development efforts are ongoing toward further enhancement of the instrument. In the future, more advanced algorithms can be developed based on the high-resolution muon track data. Specifically, the energy spectrum model at large incident angles requires further investigation. The current angular resolution significantly exceeds the requirements for muon transmission radiography. This suggests that for future high spatial-resolution detector applications, the distance between detectors can be shortened. A reduced inter-detector distance would enable the instrument to achieve a larger field of view, thereby increasing the muon rate.

ACKNOWLEDGMENTS

This work was financially supported in part by the National Natural Science Foundation of China (NSFC) for Distinguished Young Scholars under Grant No. 12025504, in part by the National Natural Science Foundation of China (NSFC) for Young Scientists under Grant No. 12205297, and in part by the University of Science and Technology of China.

The authors would like to express their sincere gratitude to Yong Zhou, Sicheng Wen, Han Han, Xing Xu, Haibin Fei, Bo Wang, Mujun Li, Jiale Gao, and Xiaozhao Cao from Jianwei Scientific Instruments (Anhui) Technology Co., Ltd. for their help in detector manufacturing, instrument construction, and experiment deployment.

The authors also extend their appreciation to China Construction Eighth Engineering Division Corp., Ltd. for their assistance with the experimental site in the subway tunnel.

The authors are grateful to Haigang Zheng, Hongbo Sun, and Xiao Liang from the Anhui Earthquake Agency for their support at the Dashu Mountain experimental site.

AUTHOR DECLARATIONS

Conflict of Interest

The authors have no conflicts to disclose.

Author Contributions

Yu Wang: Conceptualization (equal); Data curation (equal); Formal analysis (equal); Funding acquisition (equal); Investigation (equal); Methodology (equal); Project administration (equal); Resources (equal); Software (equal); Supervision (equal); Validation (equal); Visualization (equal); Writing – original draft (lead); Writing – review & editing (lead). **Shubin Liu:** Conceptualization (equal); Formal analysis (equal); Funding acquisition (equal); Investigation (equal); Project administration (equal); Resources (equal);

Supervision (equal); Writing – review & editing (equal). **Zhihang Yao:** Conceptualization (equal); Data curation (equal); Investigation (equal); Methodology (equal); Resources (equal); Software (equal); Visualization (equal); Writing – original draft (equal). **Yulin Liu:** Data curation (equal); Investigation (equal); Methodology (equal). **Zhiyong Zhang:** Conceptualization (equal); Data curation (equal); Funding acquisition (equal); Investigation (equal); Project administration (equal). **Zhengyang He:** Conceptualization (equal); Data curation (equal); Methodology (equal). **Ziwen Pan:** Conceptualization (equal); Data curation (equal); Formal analysis (equal); Investigation (equal); Methodology (equal); Resources (equal). **Changqing Feng:** Conceptualization (equal); Data curation (equal); Formal analysis (equal); Funding acquisition (equal); Supervision (equal); Writing – review & editing (equal).

DATA AVAILABILITY

The data that support the findings of this study are available from the first author and the corresponding author upon reasonable request.

REFERENCES

[1]S. Procureur, Nucl. Instrum. Methods Phys. Res., Sect. A **878**, 169 (2018).
[2]M. Gottowik, "CORSIKA 8: A modern and universal framework for particle cascade simulations," arXiv:2508.08755 (2025).
[3]D. Pagano, G. Bonomi, A. Donzella, A. Zenoni, G. Zumerle, and N. Zurlo, Nucl. Instrum. Methods Phys. Res., Sect. A **1014**, 165732 (2021).
[4]L. Bonechi, M. Bongi, D. Fedele, M. Grandi, S. Ricciarini, and E. Vannuccini, in *29th International Cosmic Ray Conference* (IUPAP, 2005), Vol. 9, p. 283.
[5]T. K. Gaisser, *Cosmic Rays and Particle Physics* (Cambridge University Press, 1991).
[6]E. V. Bugaev, A. Misaki, V. A. Naumov, T. S. Sinegovskaya, S. I. Sinegovsky, and N. Takahashi, Phys. Rev. D **58**, 054001 (1998).
[7]T. Hebbeker and C. Timmermans, Astropart. Phys. **18**, 107 (2002).
[8]J. Marteau, J. d. B. d'Ars, D. Gibert, K. Jourde, J.-C. Ianigro, and B. Carlus, J. Instrum. **12**, C02008 (2017).
[9]E. George, Commonw. Eng. **42**, 445–447 (1955).
[10]L. W. Alvarez, J. A. Anderson, F. E. Bedwei, J. Burkhard, A. Fakhry, A. Girgis, A. Goneid, F. Hassan, D. Iverson, G. Lynch, Z. Miligy, A. H. Moussa, M. Sharkawi, and L. Yazolino, Science **167**, 832 (1970).
[11]K. Kazahaya, H. Shinohara, and G. Saito, Earth Planets Space **54**, 327 (2002).
[12]H. K. M. Tanaka, T. Uchida, M. Tanaka, M. Takeo, J. Oikawa, T. Ohminato, Y. Aoki, E. Koyama, and H. Tsuji, Geophys. Res. Lett. **36**, https://doi.org/10.1029/2008GL036451 (2009).
[13]L. Bonechi, F. Ambrosino, L. Cimmino, R. D'Alessandro, G. Macedonio, B. Melon, N. Mori, P. Noli, G. Saracino, P. Strolin, F. Giudicepietro, M. Martini, M. Orazi, and R. Peluso, EPJ Web Conf. **182**, 02015 (2018).
[14]D. Lo Presti, F. Riggi, C. Ferlito, D. L. Bonanno, G. Bonanno, G. Gallo, P. La Rocca, S. Reito, and G. Romeo, Sci. Rep. **10**, 11351 (2020).
[15]G. Liu, K. Yao, F. Niu, Z. Li, H. Tian, J. Li, X. Luo, L. Jin, J. Gao, J. Rong, Z. Fu, Y. Kang, W. Zhang, S. Ding, Y. Wang, J. Zeng, X. Luo, X. Tian, W. Shi, J. Hu, Z. Zhang, M. Yu, F. Wu, J. Chen, J. Liu, and Z. Liu, Geophys. J. Int. **237**, 588 (2024).
[16]R. Nishiyama, A. Ariga, T. Ariga, S. Käser, A. Lechmann, D. Mair, P. Scampoli, M. Vladymyrov, A. Ereditato, and F. Schlunegger, Geophys. Res. Lett. **44**, 6244, https://doi.org/10.1002/2017GL073599 (2017).
[17]R. Nishiyama, A. Ariga, T. Ariga, A. Lechmann, D. Mair, C. Pistillo, P. Scampoli, P. G. Valla, M. Vladymyrov, A. Ereditato, and F. Schlunegger, Sci. Rep. **9**, 6970 (2019).
[18]T. Beni, D. Borselli, L. Bonechi, D. Brocchini, S. Guideri, S. Gonzi, T. Carlà, G. Gigli, L. Lombardi, M. Nocentini, V. Ciulli, R. D'Alessandro, and N. Casagli, Eng. Geol. **353**, 108141 (2025).
[19]K. Jourde, D. Gibert, J. Marteau, J. de Bremond d'Ars, S. Gardien, C. Girerd, and J.-C. Ianigro, Sci. Rep. **6**, 23054 (2016).
[20]*Cosmic Ray Muography*, edited by P. Scampoli and A. Ariga (World Scientific Publishing Company, 2023).
[21]K. Morishima, M. Kuno, A. Nishio, N. Kitagawa, Y. Manabe, M. Moto, F. Takasaki, H. Fujii, K. Satoh, H. Kodama, K. Hayashi, S. Odaka, S. Procureur, D. Attié, S. Bouteille, D. Calvet, C. Filosa, P. Magnier, I. Mandjavidze, M. Riallot, B. Marini, P. Gable, Y. Date, M. Sugiura, Y. Elshayeb, T. Elnady, M. Ezzy, E. Guerriero, V. Steiger, N. Serikoff, J.-B. Mouret, B. Charlès, H. Helal, and M. Tayoubi, Nature **552**, 386–390 (2017).
[22]M. Niculescu-Oglinzanu, D. Stanca, A. Bălăceanu, M. Dobre, A. Gherghel-Lascu, A. Saftoiu, R. Smău, and C. Vancea, J. Appl. Phys. **136**, 174501 (2024).
[23]G. Baccani, L. Bonechi, D. Borselli, R. Ciaranfi, L. Cimmino, V. Ciulli, R. D'Alessandro, C. Fratticioli, B. Melon, P. Noli, G. Saracino, and L. Viliani, J. Instrum. **13**, P11001 (2018).
[24]A. Anastasio, F. Ambrosino, D. Basta, L. Bonechi, M. Brianzi, A. Bross, S. Callier, F. Cassese, G. Castellini, R. Ciaranfi, L. Cimmino, R. D'Alessandro, B. De Fazio, C. de La Taille, F. Garufi, G. Iacobucci, M. Martini, V. Masone, C. Mattone, S. Miyamoto, M. Montesi, R. Nishiyama, P. Noli, M. Orazi, L. Parascandolo, G. Passeggio, R. Peluso, A. Pla-Dalmau, L. Raux, R. Rocco, P. Rubinov, G. Saracino, E. Scarlini, G. Scarpato, G. Sekhniaidze, O. Starodubtsev, P. Strolin, A. Taketa, H. Tanaka, M. Tanaka, and T. Uchida, Nucl. Instrum. Methods Phys. Res., Sect. A **718**, 134 (2013).
[25]M. D'Errico, F. Ambrosino, G. Baccani, L. Bonechi, M. Bongi, A. Bross, R. Ciaranfi, L. Cimmino, V. Ciulli, R. D'Alessandro, F. Giudicepietro, S. Gonzi, G. Macedonio, V. Masone, B. Melon, N. Mori, M. Orazi, G. Passeggio, R. Peluso, A. Pla-Dalmau, G. Saracino, G. Scarpato, P. Strolin, E. Vertechi, and L. Viliani, J. Phys.: Conf. Ser. **2374**, 012190 (2022).
[26]L. Bonechi, R. D'Alessandro, and A. Giammanco, Rev. Phys. **5**, 100038 (2020).
[27]S. Bouteille, D. Attié, P. Baron, D. Calvet, P. Magnier, I. Mandjavidze, S. Procureur, M. Riallot, and M. Winkler, Nucl. Instrum. Methods Phys. Res., Sect. A **834**, 223 (2016).
[28]S. Procureur, R. Dupré, and S. Aune, Nucl. Instrum. Methods Phys. Res., Sect. A **729**, 888 (2013).
[29]B.-X. Qi, S.-B. Liu, H. Ji, Z.-T. Shen, S.-Y. Ma, H.-B. Liu, W.-Q. Huang, and Q. An, Chin. Phys. C **40**, 056102 (2016).
[30]S. Bouteille, D. Attié, P. Baron, D. Calvet, P. Magnier, I. Mandjavidze, S. Procureur, and M. Riallot, Nucl. Instrum. Methods Phys. Res., Sect. A **834**, 187 (2016).
[31]G. Yuan, S. Liu, B. Qi, C. Feng, and S. Ma, IEEE Trans. Nucl. Sci. **64**, 1346 (2017).
[32]Y. Wang, S. Liu, H. Zhuang, Z. Ding, Z. Yao, C. Feng, and Z. Zhang, IEEE Trans. Nucl. Sci. **72**, 765 (2025).
[33]J. Feng, Z. Zhang, J. Liu, B. Qi, A. Wang, M. Shao, and Y. Zhou, "Nucl. Instrum. Methods Phys. Res., Sect. A **989**, 164958 (2021).
[34]D. Zhu, S. Liu, C. Feng, C. Li, J. Dong, H. Chen, Z. Chen, and J. Pan, IEEE Trans. Nucl. Sci. **66**, 1123 (2019).
[35]S. Anvar, P. Baron, B. Blank, J. Chavas, E. Delagnes, F. Druillole, P. Hellmuth, L. Nalpas, J. L. Pedroza, J. Pibernat, E. Pollacco, A. Rebii, and N. Usher, in *2011 IEEE Nuclear Science Symposium Conference Record* (IEEE, 2011), pp. 745–749.
[36]D. Baudin, D. Attié, P. Baron, D. Bernard, D. Calvet, A. Delbart, Y. Geerebaert, and P. Gros, Nucl. Instrum. Methods Phys. Res., Sect. A **912**, 66 (2018).
[37]J. Liu, Y. Wang, C. Feng, S. Liu, and Q. Chen, J. Instrum. **20**, T05002 (2025).